Classification of Hemilabile Ligands Using Machine Learning

Ilia Kevlishvili[1], Chenru Duan[1,2], and Heather J. Kulik[1,2]*

[1]*Department of Chemical Engineering, Massachusetts Institute of Technology, Cambridge, MA 02139, USA*

[2]*Department of Chemistry, Massachusetts Institute of Technology, Cambridge, MA 02139, USA*

*Corresponding Author email:hjkulik@mit.edu

ABSTRACT: Hemilabile ligands have the capacity to partially disengage from a metal center, providing a strategy to balance stability and reactivity in catalysis, but are not straightforward to identify. We identify ligands in the Cambridge Structural Database (CSD) that have been crystalized with distinct denticities and are thus identifiable as hemilabile ligands. We implement a semi-supervised learning approach using a label-spreading algorithm to augment a small negative set that is supported by heuristic rules of ligand and metal co-occurrence. We show that a heuristic based on coordinating atom identity alone is not sufficient to identify whether a ligand is hemilabile and our trained machine-learning classification models are instead needed to predict whether a bi-, tri-, or tetradentate ligand is hemilabile with high accuracy and precision. Feature importance analysis on our models show that the second, third, and fourth coordination spheres all play important roles in ligand hemilability.

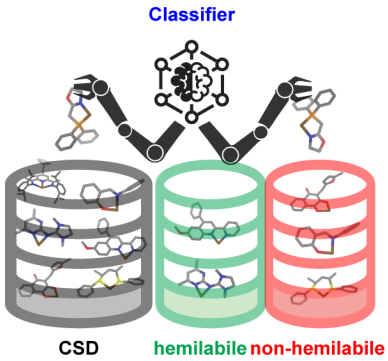

A common design principle in catalysis that can affect both reactivity[1] and selectivity[2,3] is the identity of active species and metal ligation state. Ligands that dynamically change the metal coordination environment, i.e., hemilabile ligands, are often able to address the tradeoff between catalyst activity and stability[4,5] because they can ligate and protect the transition metal while partially disengaging and making a catalytic site amenable for a reaction. Hemilabile ligands have been used to address major challenges in organic chemistry, such as reactivity selectivity tradeoffs in enantioselective[6-9], regioselective[10], and chemoselective[11] catalysis. While hemilabile ligands have been primarily used in homogeneous catalysis, their unique properties have also been utilized in nanoparticle[12], single atom[13], and heterogeneous catalysis[14,15] in recent years.

Normally, new reaction design or reactivity improvement involves screening a large number of ligands[16-18] or performing computational mechanistic studies[19-23]. While ligand hemilability is often used as a design principle[9,21,24], such a principle mainly relies on a set of heuristic rules such as distinct donor properties of coordinating atoms[25], flexibility of the linker between coordination atoms[24], and steric crowding[9] near the transition metal. Determining whether or not a ligand is hemilabile in solution usually requires indirect kinetic measurements of reaction rates[26-28], trapping of distinct complexes in crystal structures[29], or time-consuming computational mechanistic studies[8]. Most commonly, the design of ligands involves the trial-and-error changing and mismatching of the donor properties of coordinating atoms[25,28] in an attempt to bias ligands towards hemilability. However, symmetric, homo-functional ligands have also been shown to undergo hemilabile coordination changes[8,30,31], while some multifunctional ligands do not tend to change coordination environments[24]. Therefore, being able to tell *a priori* whether a ligand can act as a hemilabile ligand would greatly accelerate screening efforts.

Here, we employed a data-driven approach to identify factors that determine the likelihood of a ligand to be hemilabile. Data-driven approaches that can be used for prescreening suitable homogeneous catalysts with desirable properties have become increasingly common recently[32-37]. We curated a dataset of ligands from the Cambridge Structural Database (CSD). Using experimental datasets such as those from the CSD offers an advantage over hypothetical datasets because studied complexes and ligands are synthesizable. However, such an approach can suffer from experimental bias towards certain metal/ligand scaffolds that could influence trained models. We separately identified candidate hemilabile ligands from this CSD set and then used the frequent occurrence of a single, consistent denticity to assign ligands as having a high probability of being non-hemilabile. We trained machine learning (ML) procedures to predict ligand hemilability and used feature analysis of the trained models to show why common heuristic rules can struggle to fully account for hemilabile character. This ML model allowed us to further expand and suggest a set of candidate hemilabile ligands from existing (i.e., in the CSD) and thus synthesizable ligands.

We first curated a dataset of hemilabile ligands from a set of all ligands that appear in mononuclear transition metal complex (TMC) crystal structures[38 39]. We identified 4,144 ligands that appear in mononuclear TMCs with different denticities, with their highest-denticity conformations ranging from bidentate to nonadentate, based on the molecular graph determinants of each ligand bound to a dummy transition metal[40], as well as those of ligands with transition metal absent (Supporting Information Text S1). A ligand was labeled hemilabile if the molecular graph determinant of a ligand without the transition metal mapped to more than one molecular graph determinant of a ligand bound to a transition metal, indicating a change in the coordination environment (Figure 1, inset). We separated these ligands into distinct subsets based on the highest denticity of the ligand. Because bi-, tri-, and tetradentate ligands are most widely used for catalysis

and were the most common ligand types among those identified as hemilabile, only these ligands were studied further (Figure 1 and Supporting Information Figures S1–S2). To focus on catalytically relevant ligand types and remove trivial cases arising from agostic interactions[41] such as those with hydrogen, we eliminated any ligands where the coordinating atoms did not consist of carbon, nitrogen, oxygen, phosphorus, or sulfur (Supporting Information Table S1). Finally, any ligands with a high absolute charge, q, assignment (i.e., $|q|$ >4) were eliminated in order to remove ligands derived from either highly charged or poorly resolved (i.e., missing hydrogen atoms) complexes (Supporting Information Table S1). After each of these steps, we obtained a set of 1,531 hemilabile bidentate, 1,069 tridentate, and 492 tetradentate ligands.

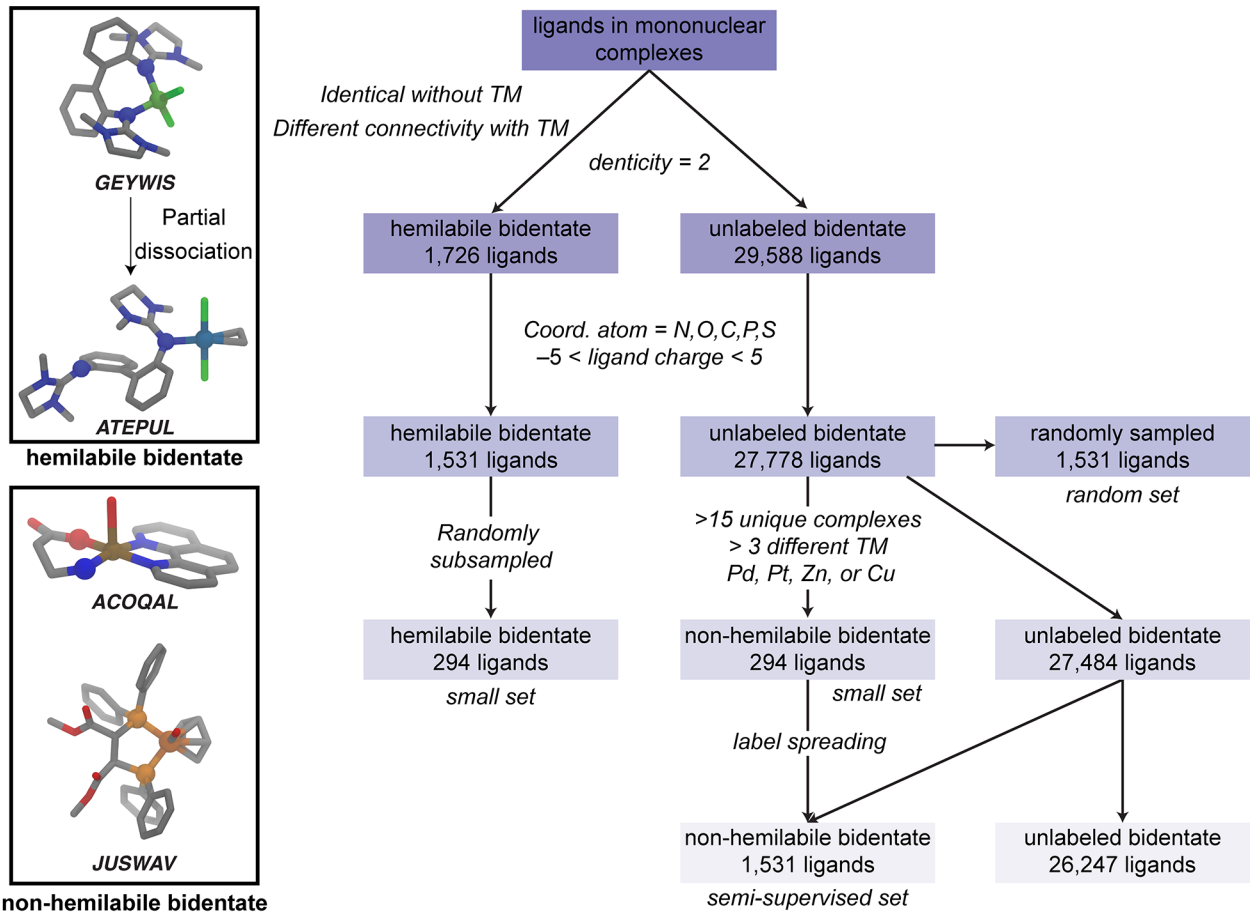

Figure 1. Description of the data curation workflow and filtering steps for defining bidentate hemilabile and non-hemilabile sets. Examples of a hemilabile ligand in high- and low-denticity conformations are shown in the top inset, along with refcodes (**GEYWIS** – Ni, **ATEPUL** – Pd)

associated with a representative complex involving other non-hemilabile ligands, where ligating atoms of the hemilabile ligand and the transition metal are shown as spheres. Examples of non-hemilabile ligands are shown in the bottom inset (**ACOQAL** – Cu, **JUSWAV** – Fe). Hydrogens are omitted for clarity. Atoms in the insets are colored as follows: C in gray, O in red, N in blue, Ni in dark green, Cl in green, Pd in light blue, Cu in brown, P in light orange, Fe in dark orange.

To gain insight into how the identity of the transition metal affects the conformation of a complexed hemilabile ligand, we analyzed how frequently each of the 4,144 hemilabile ligands appear with the ten most common transition metals in their lowest- and highest-denticity conformations (Supporting Information Figure S3). We find that while most transition metals tend to favor the higher-denticity conformation of a hemilabile ligand, ligands that appear in complexes with palladium, platinum, and zinc tend to prefer a lower-denticity conformation. We also find that among the metals studied, a hemilabile ligand has the highest likelihood of being crystallized in complex with Cu in both high- and low-denticity conformations. The majority (55%) of hemilabile ligands appear in both high and low denticities in at least two distinct complexes with the same transition metal center. Nevertheless, this means that a significant number of ligands only appear in different denticity conformations when the identity of the transition metal is changed (Supporting Information Table S2). While transition metal identity can play an important role in determining ligand hemilability, the limited sizes of the datasets prevented us from further studying metal-dependent properties.

To ensure we avoid introducing bias in our hemilabile ligand dataset by including ligands that strongly prefer either high- or low-denticity conformations, we evaluated how many times they appear in each denticity in the unique complexes of these ligands (Supporting Information Figures S4–S6). While different denticity changes are possible for hemilabile tridentate (e.g., to bidentate or monodentate) and tetradentate ligands (e.g., to bidentate), here we define only two

classes, i.e., hemilabile and non-hemilabile, to ensure sufficient data for each class (Supporting Information Figures S7–S8). There is a wide distribution of the hemilabile ligands occurring in the low-denticity configuration relative to the total occurrences that is nevertheless centered around 0.5 (i.e., both low and high denticity are equally weighted). For the majority of ligands (i.e., 75.8% bidentate, 75.4% tridentate, 76.8% tetradentate), the ratio of low denticity to total count is between 0.2 and 0.8, indicating that these hemilabile ligands appear in higher- and lower-denticity conformations with similar frequency. Only a very minor fraction of ligands (i.e., 1.2% bidentate, 0.6% tridentate, 0.8% tetradentate) strongly prefer either high- or low-denticity conformations (i.e., the ratio of low denticity to total count is < 0.01 or > 0.99). Thus, most ligands in our hemilabile set can be expected to sample both denticities based on their occurrence in crystal structures.

Using this dataset of hemilabile ligands, we next devised a strategy to train machine learning (ML) models that could predict the likelihood of a ligand to exhibit hemilability for bidentate ligands. To train such a model, we require not just the hemilabile ligand dataset but also a set of non-hemilabile ligands to serve as the negative class. Although positive examples of hemilability are identifiable based on the presence of complexes with ligands in multiple denticities, the absence of multiple denticities for ligands across complexes could be due to a lack of diversity of synthesized complexes containing a given ligand rather than to a lack of hemilabile ligand character. To address this issue, we defined three different non-hemilabile sets. First, we randomly subsampled all unlabeled bidentate ligands (i.e., those not positively identified as hemilabile in the preceding analysis) to obtain an equal number of probable non-hemilabile ligands as labeled hemilabile ligands (random dataset, Figure 1). Next, we used a small set of ligands with an expected lack of hemilability supported by frequent and diverse appearance in the CSD with a

single denticity (small dataset, Figure 1 and see Supporting Information Text S2). Finally, we used a semi-supervised learning strategy that augments the small non-hemilabile dataset by using machine learning to identify more non-hemilabile ligands (semi-supervised dataset, Figure 1 and Supporting Information Text S2). Semi-supervised learning[42] encompasses a broad set of techniques that combine aspects of supervised (i.e., with labeled data) and unsupervised (i.e., with unlabeled data) learning approaches to address the challenges of partially labeled datasets. This approach enables construction of a model that can benefit from the large size of the known-hemilabile set while preserving good labels for non-hemilabile ligands. We used these datasets to train classification models using the extreme gradient boosting algorithm[43] (XGBoost) for the prediction of hemilability (Figure 1). To featurize ligands, we used ligand-based revised autocorrelations (RACs)[44], which are connectivity-based representations that have been successfully applied to transition metal complex property prediction[44-47] (see Computational Details).

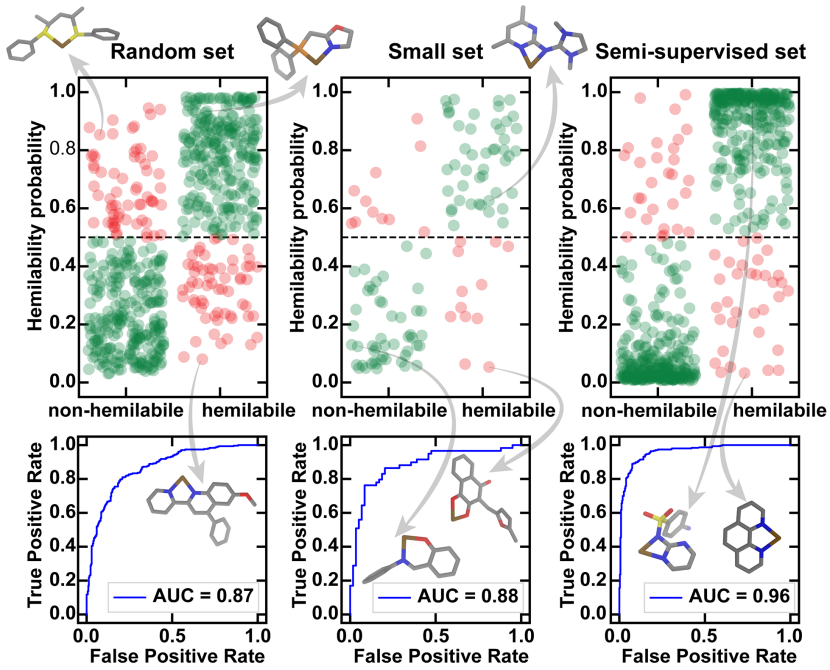

Figure 2. ML classifier (i.e., XGBoost) prediction probability (top) and ROC for random (left), small (middle), and semi-supervised (right) datasets. All data points are represented as translucent

circles to depict data density and colored by classification correctness: correct (green) and incorrect (red). Examples of correct and incorrect classifications of ligands are shown as insets, bound to a metal. Hydrogens are omitted for clarity. Atoms are colored as C in gray, N in blue, O in red, P in orange, S in sulfur, and metal in brown.

The model trained on the randomly subsampled dataset shows promising performance on a set-aside test set with good separation between two classes with a receiver-operating characteristic area under the curve (ROC-AUC) of 0.86 as well as good accuracy (0.80) and recall (0.80), despite our expectation of potential label contamination due to incorrectly assigned negative labels (Figure 2 and Supporting Information Figures S9–S10 and Table S3). Despite a significantly diminished training set size for the small dataset (i.e., an 80% training partition of 3,062 ligands versus 588 ligands in the small set), the model trained on this dataset shows a slight improvement over the randomly sampled set in terms of its predictive power on the test set, including an improved ROC-AUC of 0.88, accuracy of 0.81, and a comparable recall of 0.80 (Figure 2 and Supporting Information Figures S11–S12 and Table S3). Finally, we trained an ML model classifier (i.e., again XGBoost) using the full set of identified hemilabile ligands and a size-matched negative class made up of the small set of non-hemilabile ligands augmented by label spreading. While the majority of the negative, non-hemilabile class was defined using the semi-supervised augmentation technique, the set of hemilabile ligands remained unchanged. Therefore, to ensure that the hemilabile ligands in the test set were unseen during the augmentation approach, label spreading approach was implemented using only the hemilabile ligands in the training set (i.e., 80%), and the set-aside hemilabile ligands were used to construct the test set for the final model. This model shows by far the best overall performance, with a marked improvement that includes an ROC-AUC of 0.96, accuracy of 0.90, and recall of 0.89 (Supporting Information Figures S13–S14 and Table S3).

In order to test the limits of this encouraging performance, we carried out a more stringent test of a grouped split in which we nearly eliminated specific coordinating atom elements from the training set. Specifically, we removed 90% of the ligands that contained at least one phosphorus atom as a coordinating atom from the entire dataset and defined a new test set that only contained ligands with at least one phosphorus atom as a coordinating atom. This split largely preserves our label balance (i.e., 51:49 hemilabile:non-hemilabile in training and 45:55 in the test set). Although performance is expectedly reduced, this model still shows encouragingly good performance, including an ROC-AUC of 0.94, accuracy of 0.87, and a recall of 0.84 (Supporting Information Figures S15–S17 and Table S3).

Given the good performance we observed on bidentate hemilabile ligands, we repeated our analysis and ML model training for tri- and tetradentate ligands. Given the somewhat smaller dataset sizes, we reduced the requirement for the number of unique complexes to confidently label negative examples (Supporting Information Figures S1–S2). For both tridentates and tetradentates, we trained XGBoost ML models using all three protocols we demonstrated on the bidentate set. The XGBoost ML models trained to predict the hemilability of tridentate ligands on the randomly selected set (2,138 ligands total) show relatively poor performance, with an ROC-AUC of 0.72 and accuracy of 0.67, but this is improved by using the small set (ROC-AUC of 0.79 and accuracy of 0.73, 354 ligands total) and even more substantially by using a semi-supervised set (ROC-AUC of 0.94 and accuracy of 0.87, 2,138 ligands, Figure 3 and Supporting Information Table S4). For the tetradentate models, smaller dataset sizes (984 ligands for the randomly selected set) mean that we do not see the performance improvement from the randomly selected dataset (ROC-AUC of 0.81, accuracy 0.73, and recall 0.83) to the small dataset (ROC-AUC of 0.82, accuracy of 0.75, and recall 0.77, 222 ligands total), and we attribute this comparable performance to the small size

(178 ligands) of the training set (Figure 3 and Supporting Information Table S5). Thus, the semi-supervised approach is particularly critical in this case, giving by far the best model performance (ROC-AUC of 0.97, accuracy of 0.93, and recall 0.96). We also carried out the same grouped split test for tri- and tetradentate ligands, but we held out oxygen for tetradentate ligands due to both the limited number and class imbalance of phosphorus-coordinating ligands among the tetradentate set. These grouped split models using the semi-supervised labeled data still show good performance, with ROC-AUC of 0.88 and 0.92 for tri- and tetradentate ligands, respectively. To confirm the approach is not strongly sensitive to the ML model, we also trained support vector classifiers, random forest models, and multilayer perceptron models that all have comparable performance to the XGBoost model across all three ligand types (Supporting Information Tables S6–S8).

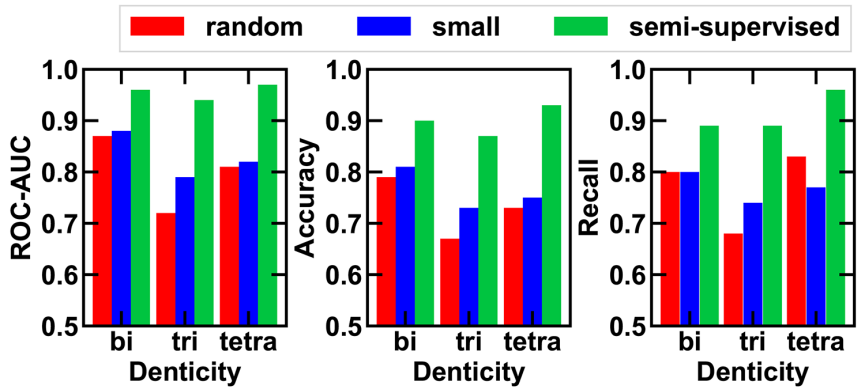

Figure 3. Accuracy and recall of the XGBoost classifier model on the test sets of random, small, and semi-supervised sets.

We next aimed to understand what chemical mapping emerged during the development of the non-hemilabile ligand set via label spreading by comparing differences in chemical and structural diversity of the two classes. We first analyzed the coordination environment of these ligands and calculated common geometric features of ligands bound to a representative transition

metal center (here, copper) in their highest-denticity conformations. Analysis of the coordination atom environment shows some differences and similarities between the two labeled sets in the total semi-supervised dataset (Figure 4). As expected, hetero-donating ligands, where the identity of coordinating ligands differ, are more common among hemilabile ligand sets, which is a common design principle for hemilability. However, the non-hemilabile ligand set also features many hetero-donating ligands. Furthermore, homo-donating ligands are still frequent in the hemilabile ligand set. In particular, the hemilabile ligand set shows a higher number of bis-oxygen coordinating configurations, which can be attributed to the generally weaker donor ability of oxygen-coordinating ligands. While bis-nitrogen ligands are more common among non-hemilabile sets, they are still abundant within hemilabile sets. Analysis of ligand charges shows that the majority of ligands in the dataset are neutral both for hemilabile and non-hemilabile ligands, revealing that charges alone cannot distinguish between the two classes (Supporting Information Figure S18). From the geometric analysis, we find that hemilabile ligands tend to have a slightly lower steric crowding near the metal based on the common steric descriptors such as buried volume[48] or solvent-accessible surface area[49], which can be attributed to the decrease in ligand bite angle and weaker binding to the transition metal, based on the metal–ligand bond distances (Supporting Information Figures S19–S23). The overlap of the distributions of these simple descriptors highlights the difficulty of distinguishing hemilabile ligands from non-hemilabile ligands, necessitating more complex classification models.

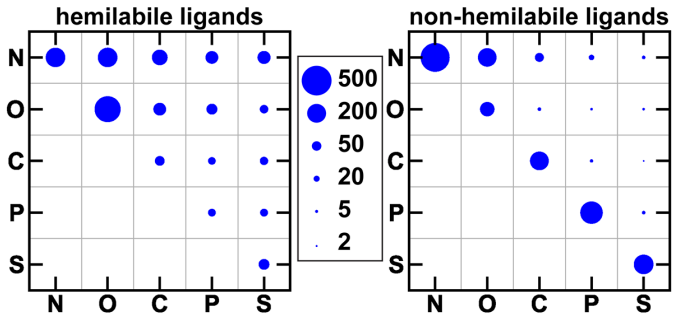

Figure 4. Upper triangular coordinating atom matrix showing the frequency of different coordinating environments observed in the hemilabile (left) and non-hemilabile ligand datasets of bidentate ligands. The area of each circle represents the total count of unique ligands, as indicated qualitatively by the inset legend.

Analysis of the coordinating atom environment of tri- and tetradentate ligands shows that, similar to the bidentate ligands, the frequency of hetero-donating ligands is higher within the hemilabile set (Supporting Information Figures S24–S25). Unlike the bidentate set, we find that the all-nitrogen-donating ligand becomes the predominant class not only for the non-hemilabile ligand set but also for the hemilabile ligand set. Similarly, we see an increase in the total number of oxygen-donating ligands in the hemilabile class, which can be attributed to weaker donor strength of oxygen-donating ligands. Furthermore, there is a marked increase in the number of bis-carbon donating ligands among the hemilabile set for both tri- and tetradentate ligands, which can be attributed to the π-coordinating alkene ligands, with a C=C bond forming a coordination geometry that our method assigns as bidentate. Although monodentate might be a more suitable classification for these metal-ligand interactions, this choice is only relevant to our model training if such ligands can also form higher denticity (i.e., tridentate) coordinating geometries, which is not expected. Thus, this choice is unlikely to influence model development. Neutral ligands are also still the most common in tridentate and tetradentate sets, with a somewhat increased bias towards charged ligands introduced in the non-hemilabile set (Supporting Information Figures

S26–S27). Similar to the bidentate ligand set, steric crowding around non-hemilabile ligands tends to be lower (Supporting Information Figures S28–S29). The consistent trends between ligand types demonstrate the internal consistency of our label assignment, however pervasive overlap between the two classes demonstrates the difficulty of identifying hemilabile ligands the need for classification models.

Although our ML models perform well at predicting whether or not a ligand will demonstrate hemilability in the context of CSD structures, validating these predictions in the context of homogenous catalysis would require difficult experiments. As an alternative strategy to validate our models, we carried out electronic structure calculations with density functional theory (DFT) to discern differences in ligand dissociation energies between our hemilabile and non-hemilabile (i.e., either from the small or semi-supervised) ligands. We selected 100 total tridentate ligands that were neutral (i.e., to avoid issues with charge separation during dissociation) and had been crystalized with Cu in the CSD. In total, 50 tridentate ligands were obtained from the hemilabile set, and 50 tridentate ligands were from the non-hemilabile set (25 small, 25 semi-supervised). A complete list of the ligand refcodes and structures of the ligands are provided in the Supporting Information. We selected tridentate ligands for this test because tridentate ligands were the most challenging for our ML models to classify. The focus on copper is motivated by the fact that copper is the metal with the highest frequency in which we also have a high likelihood of finding a ligand in both high- and low-denticity binding configurations. We constructed complexes with the hemilabile or non-hemilabile ligand bound to a Cu complex that also contained chloride, in a four-coordinate tetrahedral or square planar geometry, depending on the ligand geometry. We computed partial dissociation energies of the three Cu–L bonds in these complexes. For these partial ligand dissociation energies (see Computational Methods) we observe that partial ligand

dissociation is more favorable for hemilabile ligands, with a mean partial dissociation energy of –1.8 kcal/mol for the bidentate configuration relative to the tridentate bound conformation, whereas the partial dissociation energy of non-hemilabile ligands was found to be 2.3 kcal/mol, implying that the partial dissociation is more favorable for the hemilabile set (Supporting Information Figures S30–S31). Independent t-test analysis showed that these two sets have distinguishable population means, whereas the same test applied to the two non-hemilabile sets does not support a significant difference between the populations (Supporting Information Table S9). Furthermore, 42 out of 50 hemilabile ligands were found to have a partial dissociation energy below 1.5 kcal/mol, suggesting that these complexes should be highly hemilabile with both high and low denticity complexes existing in equilibrium. Thus, our semi-supervised labeling strategy quantitatively distinguishes hemilabile and non-hemilabile ligands.

Motivated by our observation of good ML model performance in classifying ligands capable of demonstrating hemilability, we further analyzed what features our models emphasize in making this classification. We carried out a feature importance analysis of the final XGBoost model by examining the total gain function of each feature, where we only considered features that contributed at least 1% to the total gain. Our feature set contains both full-scope ligand features that are related to global properties, as well as coordinating atom-centered features, that encompass more metal local 1st and 2nd coordination shells (d = 0 and d = 1, respectively) and more metal-distal properties in 3rd and 4th coordination shells (d = 2 and d = 3, respectively). Consistent with our earlier analysis, we find that the metal-local features (i.e., 1st or 2nd coordination sphere) contribute less (i.e., 25–50%) than the more distal features (i.e., 3rd coordination sphere and global) that contribute ~50-75% to the total prediction for bidentate and tridentate ligand types (Figure 5). Conversely, a somewhat larger (~60%) contribution of metal-local features is observed

in the tetradentate model (Figure 5). We observe similar feature importances, with metal-distal features contributing ~50-75% of the total prediction using an alternative feature importance measure based on Gini impurity in a random forest classifier, and we notably observe reduced contributions from the metal-local features for tetradentates (~50%, Supporting Information Figure S32). The significant contribution of metal-distal and global features explains the difficulty associated with predicting ligand hemilability based on previously emphasized heuristics including donor ability[6,24,28,50]. Furthermore, hemilability is a highly balanced property that depends both on structural and electronic features, unlike other properties such as spin state that depend much more strongly on electronic features[44] (Figure 5).

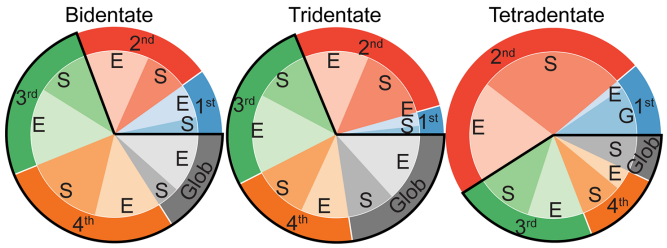

Figure 5. Feature importance of bidentate (left), tridentate (middle) and tetradentate (right) ligands based on the total gain of the XGBoost classifier. Only features that contributed more than 1% to the classifier were retained. *S* refers to structural (topology, identity, radius) and *E* refers to electronic (electronegativity, nuclear charge) features. First through fourth refers to the coordination shell relative to the transition metal based on ligand-centered RACs depth, and Glob refers to global (ligand-scope) features.

Finally, to demonstrate the promise of our ML models for ligand discovery in catalyst design, we use the best-performing XGBoost models to make hemilability predictions for all unlabeled ligands in our original dataset. Our model assigns many ligands as candidates for hemilability. For bi- and tetradentate ligands, we obtain bimodal distributions with a similar number of ligands labeled as labile and non-hemilabile, whereas the majority of the tridentate ligands are labeled as hemilabile (Figure 6). The prediction of most tridentate ligands to be hemilabile appears likely to be an overprediction of hemilability. For example, a tridentate ligand

featuring a cyclic, rigid 1,3,5-triazinane based scaffold (refcode: **AROGAQ**), is confidently (probability = 0.94) predicted to be hemilabile, even though partial dissociation would likely cause an increase in the ring strain due to conformation change from chair to twist-boat (Figure 6). These trends by ligand denticity are consistent with the performance of the classifier trained on the random set, where bidentate and tetradentate ligands showed better performance on the randomly sampled set, but the tridentate classifier had poorer performance. This suggests that negative examples were particularly difficult to assign accurately for the tridentate model and some degree of label contamination occurred even with semi-supervised learning in selecting negative samples, indicating that the model has not learned well to distinguish positive and negative examples. As a result, when applied to a new space of candidate ligands, the model is likely erroneously overpredicting hemilability on this new set.

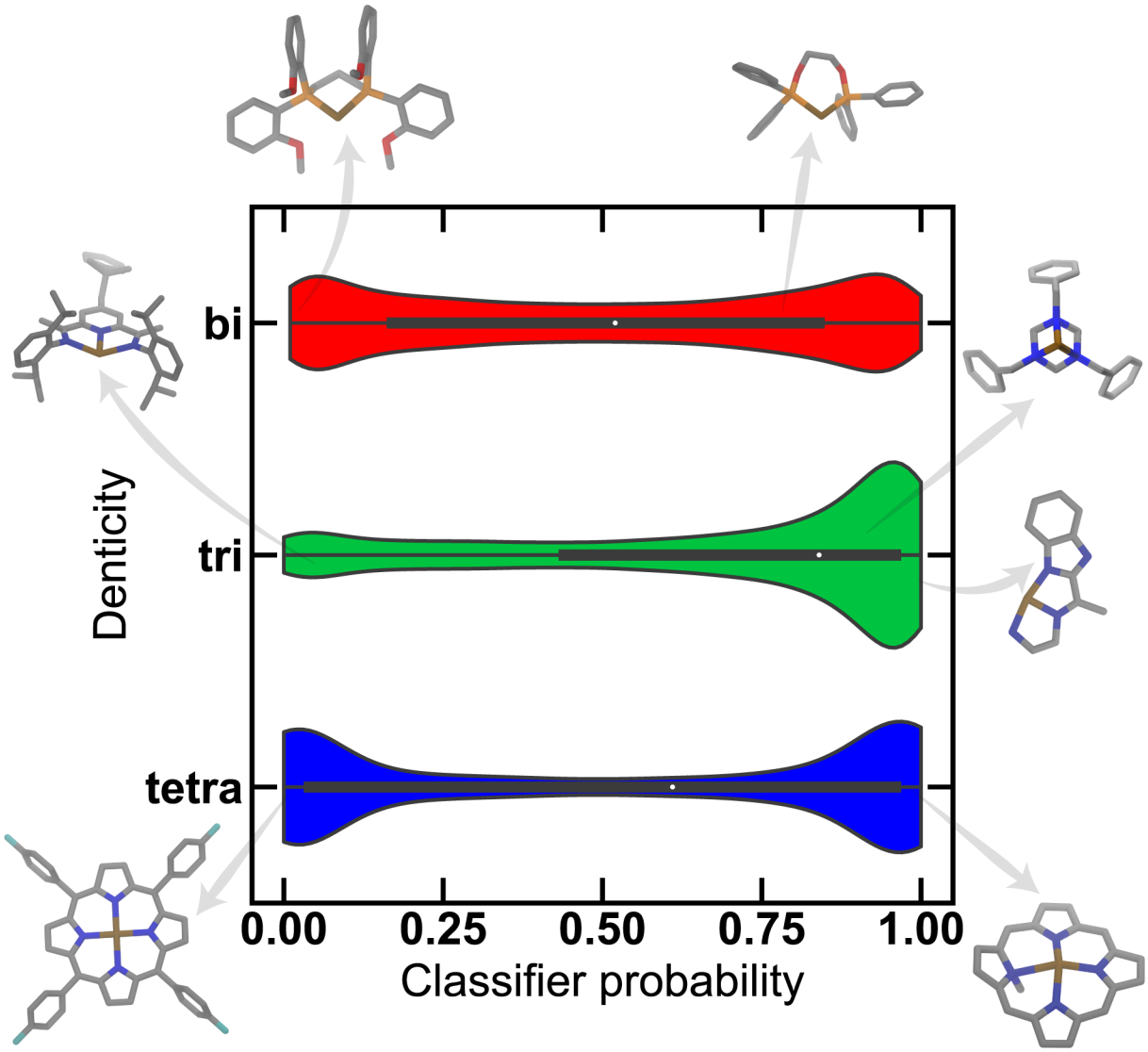

Figure 6. Distribution of the classifier probability on the unlabeled set for bidentate (red), tridentate (green), and tetradentate (blue) ligands. The total area of each distribution is scaled relative to the size of each set. Examples of hemilabile and non-hemilabile ligands within each set are shown as insets. Hydrogens are omitted for clarity. Representative ligand structures (Refcodes: **FUGCES**, **COBHIL**, **BUGVOP**, **AXOLEE**, **AROGAQ**, **BODZEA**, **CMPORZ** – clockwise starting from the bottom left corner) are shown, with atoms colored as C in gray, N in blue, O in red, P in orange, and metal in brown.

We further analyzed the predictions by the model to gain insight into the confidence we should have in its predictions and to identify where it could be used in ligand design. For example, a bidentate, bisphosphine ligand with a short, rigid linker between two coordinating atoms is

confidently classified as non-hemilabile. However, by changing the bisphosphine ligand's electronic character to bisphosphinite, which has a more flexible ethane diol linker between two coordinating atoms, the resulting ligand is classified as hemilabile (Figure 6, inset-top). Similarly, we find that the structure of a tridentate N,N,N-coordinating ligand consisting of rigid sp^2 hybridized linkages between coordinating atoms and bulky substituents that constrain movement results in the classification of non-hemilabile, whereas a ligand possessing a freely rotatable ethylene linker in place of a rigid linker is confidently classified as hemilabile (Figure 6, inset-middle). Finally, we find that certain classes of macrocyclic tetradentate ligands, such as porphyrin-derived ligands, are confidently classified as non-hemilabile. On the other hand, when one of the coordinating nitrogen atoms in such a structure is alkylated, leading to a significant reduction in its donor ability and change from an X type to an L type ligand, the classifier confidently assigns this ligand as hemilabile. While this observation is intuitive, this finding highlights how the model is sensitive to small alterations in the overall structure (Figure 6, inset-bottom). Thus, the ML models, especially those trained on bidentate and tetradentate ligands, should provide new pathways to discovering novel hemilabile ligands. We propose that tridentate model predictions could be paired with high-throughput DFT, i.e., to rule out any model-predicted hemilabile ligands that remain strongly bound to a representative metal center, to provide additional support to model predictions given limitations in tridentate dataset quality from labels obtained purely from the CSD.

In summary, we developed a data-driven workflow for identifying hemilabile to accelerate catalyst screening. We used a semi-supervised learning approach to leverage a combination of labeled and unlabeled data to confidently identify examples of non-hemilabile ligands. We trained ML models that can predict ligand hemilability for bidentate and tetradentate ligands with high

accuracy, and we also demonstrated a model for tridentate ligands with a suggested strategy for further validation using DFT. We showed that coordinating atom identity alone fails to account for ligand hemilability. Feature importance analysis of machine learning models highlights why conventional design principles can be insufficient for the identification of hemilabile ligands, due to the high significance of metal-distant and structural features. We used trained machine learning models to identify a large number of ligands that are predicted to be hemilabile and that can be used for accelerated discovery of new catalytic reactions.

Computational Methods

Dataset curation: A set of ligands present in mononuclear transition metal complexes was curated from the Cambridge Structural Database (CSD)[51] version 5.41 (November 2019). The procedure employed the Conquest graphical interface and the CSD Python API, with the v5.41 dataset including complexes from the November 2019 dataset with March 2020 and May 2020 updates. Ligand charges were determined using the octet rule charge assignment.[52] A dummy atom with identical connectivity to the metal with an atomic number of 0 was introduced to identify ligands without preserving metal identity. For each ligand with a dummy atom, the atomic number and bond-order weighted connectivity matrix determinant were calculated to identify unique ligands, including their metal–ligand connectivity, as described in ref [38]. Atomic number and bond-order weighted connectivity matrix determinant in the absence of a dummy atom was also calculated to identify the same ligands with differing transition metal connectivity.

Feature set: Ligands were featurized using ligand-based revised autocorrelations (RACs),[44] which are connectivity-based representations that have been successfully applied to transition metal complex property predictions.[44-47] Ligand-based RAC features are generated from molecular graphs of a ligand bound to the same dummy transition metal, where each atom is

represented by a vertex and each bond is represented by an unweighted edge. Each RAC feature is the sum of products or the sum of differences of heuristic atom properties at depth *d* (i.e., the number of bonds separating two atoms) on a molecular graph. The ligand-based RACs in this work include features that both span the entire ligand bound to a transition metal, where every atom is used as a starting atom in RACs, as well as features that are centered around only coordinating atoms with a maximum depth $d = 3$. A depth of $d = 3$ has been previously motivated after observing diminishing returns for higher distance cutoffs.[44] Overall, ligand-based RACs consist of 52 total features (Supporting Information Text S3 and Table S10).

Machine learning models: Three different models were trained per maximum ligand denticity (i.e., bidentate, tridentate, and tetradentate), where the assignment of negative labels was different in each case. For each model, we used the 80/20 stratified random train/test split to ensure conservation of the same ratios of positive and negative classes in the training and test set. For random and semi-supervised sets, that contain identical positive labels, the identities of the positive train/test groups were preserved. However, since negative ligands are distinct for each set, in each case, negative classes were split randomly into 80/20 train/test split. All curated training and test sets are available in the Supporting Information. We trained classification models using XGBoost v1.5.0, a gradient boosting ensemble model, to classify ligands as either hemilabile or non-hemilabile. Hyperparameters were optimized using Hyperopt v.0.2.7[53] (Supporting Information Table S11). Hyperparameters were selected on the basis of stratified three-fold cross validation of the training set with binary cross-entropy as the figure of merit. Machine learning model feature importance analysis was conducted with the feature scores of the XGBoost model based on the total gain. We employed the label-spreading semi-supervised learning approach implemented in scikit-learn[54] to identify non-hemilabile ligands. Here, the full negative class from the small set

combined with only 80% of positively labeled hemilabile ligands were used for label spreading. These hemilabile ligands are the same ligands as the ones used in the training set of random and semi-supervised sets. Ligands that were assigned to the negative class with high confidence (>0.995) based on label-spreading, were assigned a negative label. The pseudo-label set was then randomly sampled to supplement the original dataset to obtain an equal number of positive and negative examples for further examination.

Electronic structure calculations: We employed a developer version of the GPU-accelerated TeraChem v1.9[55,56] code to carry out DFT calculations. All calculations were carried out using the B3LYP[57-59] functional with the semi-empirical D3[60] dispersion correction and using Becke–Johnson damping.[61-63] The LACVP* basis set was used, employing the LANL2DZ[64] effective core potential for Cu and 6-31G* for other atoms. All calculations were carried out as closed-shell singlets in a restricted formalism. All initial geometries of ligands bound to metal were obtained from the CSD, and chloride atom was added manually, followed by universal force field[65] optimization. All structures were initially optimized to the tridentate-bound conformation with the translation rotation internal coordinate (TRIC) optimizer[66], using the BFGS algorithm with default convergence thresholds of maximum energy gradient of 4.5×10^{-4} hartree/bohr and energy difference between steps of 10^{-6} hartree. Minimas were confirmed for five representative structures using the Hessian matrix, and the Hessian matrices are provided in the Supporting Information for these complexes. To systematically calculate partial dissociation energies, we carried out a series of constrained scans, where each of the three metal–ligand bonds was extended by 2 Å from the ground state geometry, in 10 incremental steps, using the TRIC optimizer, while all other internal coordinates were allowed to relax. The final structure from the scan was used to carry out another optimization using the TRIC optimizer and same convergence threshold as

described above, which converged to a lower denticity conformation minimum. Out of the three resulting conformers, the lowest-energy conformation was chosen to calculate the partial dissociation energy.

ASSOCIATED CONTENT

Supporting Information. The identification of hemilabile ligands using molecular graph determinants; Statistics on hemilabile ligand data set curation; Workflow for defining tridentate ligand sets; Workflow for defining tetradentate ligand sets; Statistics on transition metal counts of hemilabile ligands; Frequency of hemilabile ligands to share a common transition metal; Distribution of low denticity ratio for bidentate ligands; Distribution of low denticity ratio for tridentate ligands; Distribution of low denticity ratio for tetradentate ligands; Tridentate ligand denticity in lower denticity conformations; Tetradentate ligand denticity in lower denticity conformations; Curation of non-hemilabile ligand datasets; ROC curve of XGB classifier for a randomly selected bidentate set; PR curve of XGB classifier for a randomly selected bidentate set; ROC curve of XGB classifier for a small bidentate set; PR curve of XGB classifier for a small bidentate set; Buried volume of bidentate ligands; Solvent accessible surface area of bidentate ligands; Bite angle of bidentate ligands; Metal ligand bond distances of bidentate ligands; Scaled metal ligand bond distances of bidentate ligands; ROC curve of XGB classifier for a semi-supervised bidentate set; PR curve of XGB classifier for a semi-supervised bidentate set; XGBoost classifier prediction probability on the group split set; ROC curve of XGB classifier for a bidentate group split set; PR curve of XGB classifier for a bidentate group split set; Coordinating atom matrix for tridentate ligands; Coordinating atom matrix for tetradentate ligands; Buried volume of tridentate ligands; Buried volume of tetradentate ligands; Performance metrics of XGBoost classifier on bidentate ligands; Performance metrics of XGBoost classifier on tridentate ligands; Performance metrics of XGBoost classifier on tetradentate ligands; Performance metrics of different classifiers on bidentate ligands; Performance metrics of different classifiers on tridentate ligands; Performance metrics of different classifiers on tetradentate ligands; Partial dissociation energies of tridentate ligands combined non-hemilabile; Partial dissociation energies of tridentate ligands split non-hemilabile; Independent t-test for DFT calculated partial dissociation energies; Feature importance of random forest classifier; Hyperparameters for XGBoost model; Description of RACs feature set. (PDF)

Curated datasets; DFT energies; final model predictions; models. (ZIP)

This material is available free of charge via the Internet at http://pubs.acs.org.

AUTHOR INFORMATION

Notes

The authors declare no competing financial interest.

ACKNOWLEDGMENT

This work was supported by the National Science Foundation under grant number CBET-1846426 (to I.K. and H.J.K.). Initial database development was supported by the Office of Naval Research under grant number N00014-20-1-2150 (to C.D.). H.J.K. holds an Alfred P. Sloan Fellowship in Chemistry and is the recipient of a Simon Family Faculty Research Innovation Fund, which supported this work. The authors acknowledge Adam H. Steeves for providing a critical reading of the manuscript.

REFERENCES

(1) Newman-Stonebraker, S. H.; Smith, S. R.; Borowski, J. E.; Peters, E.; Gensch, T.; Johnson, H. C.; Sigman, M. S.; Doyle, A. G. Univariate Classification of Phosphine Ligation State and Reactivity in Cross-Coupling Catalysis. *Science* **2021,** *374*, 301-308.

(2) Schoenebeck, F.; Houk, K. N. Ligand-Controlled Regioselectivity in Palladium-Catalyzed Cross Coupling Reactions. *Journal of the American Chemical Society* **2010,** *132*, 2496-2497.

(3) Palani, V.; Hugelshofer, C. L.; Kevlishvili, I.; Liu, P.; Sarpong, R. A Short Synthesis of Delavatine a Unveils New Insights into Site-Selective Cross-Coupling of 3,5-Dibromo-2-Pyrone. *Journal of the American Chemical Society* **2019,** *141*, 2652-2660.

(4) Zeng, M.; Li, L.; Herzon, S. B. A Highly Active and Air-Stable Ruthenium Complex for the Ambient Temperature Anti-Markovnikov Reductive Hydration of Terminal Alkynes. *Journal of the American Chemical Society* **2014,** *136*, 7058-7067.

(5) Weissman, H.; Shimon, L. J. W.; Milstein, D. Unsaturated Pd(0), Pd(I), and Pd(Ii) Complexes of a New Methoxy-Substituted Benzyl Phosphine. Aryl−X (X = Cl, I) Oxidative Addition, C−O Cleavage, and Suzuki−Miyaura Coupling of Aryl Chlorides. *Organometallics* **2004,** *23*, 3931-3940.

(6) Chintawar, C. C.; Bhoyare, V. W.; Mane, M. V.; Patil, N. T. Enantioselective Au(I)/Au(Iii) Redox Catalysis Enabled by Chiral (P,N)-Ligands. *Journal of the American Chemical Society* **2022,** *144*, 7089-7095.

(7) Ye, X.; Wang, C.; Zhang, S.; Tang, Q.; Wojtas, L.; Li, M.; Shi, X. Chiral Hemilabile P,N-Ligand-Assisted Gold Redox Catalysis for Enantioselective Alkene Aminoarylation. *Chemistry – A European Journal* **2022,** *28*, e202201018.

(8) Apolinar, O.; Kang, T.; Alturaifi, T. M.; Bedekar, P. G.; Rubel, C. Z.; Derosa, J.; Sanchez, B. B.; Wong, Q. N.; Sturgell, E. J.; Chen, J. S.; Wisniewski, S. R.; Liu, P.; Engle, K. M. Three-Component Asymmetric Ni-Catalyzed 1,2-Dicarbofunctionalization of Unactivated Alkenes Via Stereoselective Migratory Insertion. *Journal of the American Chemical Society* **2022,** *144*, 19337-19343.

(9) Wang, P.-F.; Yu, J.; Guo, K.-X.; Jiang, S.-P.; Chen, J.-J.; Gu, Q.-S.; Liu, J.-R.; Hong, X.; Li, Z.-L.; Liu, X.-Y. Design of Hemilabile N,N,N-Ligands in Copper-Catalyzed Enantioconvergent Radical Cross-Coupling of Benzyl/Propargyl Halides with Alkenylboronate Esters. *Journal of the American Chemical Society* **2022,** *144*, 6442-6452.
(10) Ros, A.; Estepa, B.; López-Rodríguez, R.; Álvarez, E.; Fernández, R.; Lassaletta, J. M. Use of Hemilabile N,N Ligands in Nitrogen-Directed Iridium-Catalyzed Borylations of Arenes. *Angewandte Chemie International Edition* **2011,** *123*, 11928-11932.
(11) Hale, L. V. A.; McGarry, K. A.; Ringgold, M. A.; Clark, T. B. Role of Hemilabile Diamine Ligands in the Amine-Directed C–H Borylation of Arenes. *Organometallics* **2015,** *34*, 51-55.
(12) Yan, N.; Yuan, Y.; Dyson, P. J. Nanometallic Chemistry: Deciphering Nanoparticle Catalysis from the Perspective of Organometallic Chemistry and Homogeneous Catalysis. *Dalton Transactions* **2013,** *42*, 13294-13304.
(13) Chen, Z.; Liu, Z.; Xu, X. Dynamic Evolution of the Active Center Driven by Hemilabile Coordination in Cu/Ceo2 Single-Atom Catalyst. *Nature Communications* **2023,** *14*, 2512.
(14) Peralta, R. A.; Lyu, P.; López-Olvera, A.; Obeso, J. L.; Leyva, C.; Jeong, N. C.; Ibarra, I. A.; Maurin, G. Switchable Metal Sites in Metal–Organic Framework Mfm-300(Sc): Lewis Acid Catalysis Driven by Metal–Hemilabile Linker Bond Dynamics. *Angewandte Chemie International Edition* **2022,** *61*, e202210857.
(15) Peralta, R. A.; Huxley, M. T.; Lyu, P.; Díaz-Ramírez, M. L.; Park, S. H.; Obeso, J. L.; Leyva, C.; Heo, C. Y.; Jang, S.; Kwak, J. H.; Maurin, G.; Ibarra, I. A.; Jeong, N. C. Engineering Catalysis within a Saturated in(Iii)-Based Mof Possessing Dynamic Ligand–Metal Bonding. *ACS Applied Materials & Interfaces* **2023,** *15*, 1410-1417.
(16) Blume, F.; Zemolka, S.; Fey, T.; Kranich, R.; Schmalz, H.-G. Identification of Suitable Ligands for a Transition Metal-Catalyzed Reaction: Screening of a Modular Ligand Library in the Enantioselective Hydroboration of Styrene. *Advanced Synthesis & Catalysis* **2002,** *344*, 868-883.
(17) Sun, H.-Y.; Kubota, K.; Hall, D. G. Reaction Optimization, Scalability, and Mechanistic Insight on the Catalytic Enantioselective Desymmetrization of 1,1-Diborylalkanes Via Suzuki–Miyaura Cross-Coupling. *Chemistry – A European Journal* **2015,** *21*, 19186-19194.
(18) van Dijk, L.; Haas, B. C.; Lim, N.-K.; Clagg, K.; Dotson, J. J.; Treacy, S. M.; Piechowicz, K. A.; Roytman, V. A.; Zhang, H.; Toste, F. D.; Miller, S. J.; Gosselin, F.; Sigman, M. S. Data Science-Enabled Palladium-Catalyzed Enantioselective Aryl-Carbonylation of Sulfonimidamides. *Journal of the American Chemical Society* **2023**, *145*, 20959-20967.
(19) Poree, C.; Schoenebeck, F. A Holy Grail in Chemistry: Computational Catalyst Design: Feasible or Fiction? *Accounts of Chemical Research* **2017,** *50*, 605-608.
(20) Thomas, A. A.; Speck, K.; Kevlishvili, I.; Lu, Z.; Liu, P.; Buchwald, S. L. Mechanistically Guided Design of Ligands That Significantly Improve the Efficiency of Cuh-Catalyzed Hydroamination Reactions. *Journal of the American Chemical Society* **2018,** *140*, 13976-13984.
(21) Burrows, L. C.; Jesikiewicz, L. T.; Lu, G.; Geib, S. J.; Liu, P.; Brummond, K. M. Computationally Guided Catalyst Design in the Type I Dynamic Kinetic Asymmetric

Pauson–Khand Reaction of Allenyl Acetates. *Journal of the American Chemical Society* **2017,** *139*, 15022-15032.
(22) Friederich, P.; dos Passos Gomes, G.; De Bin, R.; Aspuru-Guzik, A.; Balcells, D. Machine Learning Dihydrogen Activation in the Chemical Space Surrounding Vaska's Complex. *Chemical Science* **2020,** *11*, 4584-4601.
(23) Hopen Eliasson, S. H.; Jensen, V. R. Benefit of a Hemilabile Ligand in Deoxygenation of Fatty Acids to 1-Alkenes. *Faraday Discussions* **2019,** *220*, 231-248.
(24) Pérez García, P. M.; Ren, P.; Scopelliti, R.; Hu, X. Nickel-Catalyzed Direct Alkylation of Terminal Alkynes at Room Temperature: A Hemilabile Pincer Ligand Enhances Catalytic Activity. *ACS Catalysis* **2015,** *5*, 1164-1171.
(25) Weng, Z.; Teo, S.; Hor, T. S. A. Metal Unsaturation and Ligand Hemilability in Suzuki Coupling. *Accounts of Chemical Research* **2007,** *40*, 676-684.
(26) Knebel, W. J.; Angelici, R. J. Mechanism of Chelate Ring-Opening in Metal Carbonyl Complexes. *Inorganic Chemistry* **1974,** *13*, 627-631.
(27) Buckingham, D. A.; Clark, C. R. Kinetics and Mechanism of Ring Opening in the Hydrolysis of Cobalt(Iii) Carbonato Chelates. *Inorganic Chemistry* **1994,** *33*, 6171-6179.
(28) Bassetti, M. Kinetic Evaluation of Ligand Hemilability in Transition Metal Complexes. *European Journal of Inorganic Chemistry* **2006,** *2006*, 4473-4482.
(29) García-Antón, J.; Pons, J.; Solans, X.; Font-Bardia, M.; Ros, J. Synthesis of New Pdii Complexes Containing Thioether−Pyrazole Hemilabile Ligands − Structural Analysis by 1h and 13c Nmr Spectroscopy and Crystal Structures of [Pdcl2(Bddo)] and [Pd(Bddo)](Bf4)2 [Bddo = 1,8-Bis(3,5-Dimethyl-1-Pyrazolyl)-3,6-Dithiaoctane]. *European Journal of Inorganic Chemistry* **2002,** *2002*, 3319-3327.
(30) Duarte, F. J. S.; Poli, G.; Calhorda, M. J. Mechanistic Study of the Direct Intramolecular Allylic Amination Reaction Catalyzed by Palladium(Ii). *ACS Catalysis* **2016,** *6*, 1772-1784.
(31) Higman, C. S.; Nascimento, D. L.; Ireland, B. J.; Audörsch, S.; Bailey, G. A.; McDonald, R.; Fogg, D. E. Chelate-Assisted Ring-Closing Metathesis: A Strategy for Accelerating Macrocyclization at Ambient Temperatures. *Journal of the American Chemical Society* **2018,** *140*, 1604-1607.
(32) Durand, D. J.; Fey, N. Computational Ligand Descriptors for Catalyst Design. *Chemical Reviews* **2019,** *119*, 6561-6594.
(33) Gensch, T.; dos Passos Gomes, G.; Friederich, P.; Peters, E.; Gaudin, T.; Pollice, R.; Jorner, K.; Nigam, A.; Lindner-D'Addario, M.; Sigman, M. S.; Aspuru-Guzik, A. A Comprehensive Discovery Platform for Organophosphorus Ligands for Catalysis. *Journal of the American Chemical Society* **2022,** *144*, 1205-1217.
(34) Gallarati, S.; van Gerwen, P.; Laplaza, R.; Vela, S.; Fabrizio, A.; Corminboeuf, C. Oscar: An Extensive Repository of Chemically and Functionally Diverse Organocatalysts. *Chemical Science* **2022,** *13*, 13782-13794.
(35) Karl, T. M.; Bouayad-Gervais, S.; Hueffel, J. A.; Sperger, T.; Wellig, S.; Kaldas, S. J.; Dabranskaya, U.; Ward, J. S.; Rissanen, K.; Tizzard, G. J.; Schoenebeck, F. Machine Learning-Guided Development of Trialkylphosphine Ni(I) Dimers and Applications in Site-Selective Catalysis. *Journal of the American Chemical Society* **2023,** *145*, 15414-15424.

(36) Balcells, D.; Skjelstad, B. B. Tmqm Dataset—Quantum Geometries and Properties of 86k Transition Metal Complexes. *Journal of Chemical Information and Modeling* **2020,** *60*, 6135-6146.
(37) Sinha, V.; Laan, J. J.; Pidko, E. A. Accurate and Rapid Prediction of Pka of Transition Metal Complexes: Semiempirical Quantum Chemistry with a Data-Augmented Approach. *Physical Chemistry Chemical Physics* **2021,** *23*, 2557-2567.
(38) Arunachalam, N.; Gugler, S.; Taylor, M. G.; Duan, C.; Nandy, A.; Janet, J. P.; Meyer, R.; Oldenstaedt, J.; Chu, D. B. K.; Kulik, H. J. Ligand Additivity Relationships Enable Efficient Exploration of Transition Metal Chemical Space. *The Journal of Chemical Physics* **2022,** *157*, 184112.
(39) Nandy, A.; Taylor, M. G.; Kulik, H. J. Identifying Underexplored and Untapped Regions in the Chemical Space of Transition Metal Complexes. *The Journal of Physical Chemistry Letters* **2023,** *14*, 5798-5804.
(40) Taylor, M. G.; Yang, T.; Lin, S.; Nandy, A.; Janet, J. P.; Duan, C.; Kulik, H. J. Seeing Is Believing: Experimental Spin States from Machine Learning Model Structure Predictions. *The Journal of Physical Chemistry A* **2020,** *124*, 3286-3299.
(41) Brookhart, M.; Green, M. L. H.; Parkin, G. Agostic Interactions in Transition Metal Compounds. *Proceedings of the National Academy of Sciences* **2007,** *104*, 6908-6914.
(42) Seeger, M. "Learning with Labeled and Unlabeled Data," 2000.
(43) Chen, T.; Guestrin, C. In *Proceedings of the 22nd ACM SIGKDD International Conference on Knowledge Discovery and Data Mining*; Association for Computing Machinery: San Francisco, California, USA, 2016, DOI:10.1145/2939672.2939785 10.1145/2939672.2939785.
(44) Janet, J. P.; Kulik, H. J. Resolving Transition Metal Chemical Space: Feature Selection for Machine Learning and Structure-Property Relationships. *The Journal of Physical Chemistry A* **2017,** *121*, 8939-8954.
(45) Nandy, A.; Duan, C.; Janet, J. P.; Gugler, S.; Kulik, H. J. Strategies and Software for Machine Learning Accelerated Discovery in Transition Metal Chemistry. *Ind. Eng. Chem. Res.* **2018,** *57*, 13973-13986.
(46) Janet, J. P.; Chan, L.; Kulik, H. J. Accelerating Chemical Discovery with Machine Learning: Simulated Evolution of Spin Crossover Complexes with an Artificial Neural Network. *J. Phys. Chem. Lett.* **2018,** *9*, 1064-1071.
(47) Janet, J. P.; Gani, T. Z. H.; Steeves, A. H.; Ioannidis, E. I.; Kulik, H. J. Leveraging Cheminformatics Strategies for Inorganic Discovery: Application to Redox Potential Design. *Ind. Eng. Chem. Res.* **2017,** *56*, 4898-4910.
(48) Hillier, A. C.; Sommer, W. J.; Yong, B. S.; Petersen, J. L.; Cavallo, L.; Nolan, S. P. A Combined Experimental and Theoretical Study Examining the Binding of N-Heterocyclic Carbenes (Nhc) to the Cp*Rucl (Cp* = H5-C5me5) Moiety: Insight into Stereoelectronic Differences between Unsaturated and Saturated Nhc Ligands. *Organometallics* **2003,** *22*, 4322-4326.
(49) Eisenhaber, F.; Lijnzaad, P.; Argos, P.; Sander, C.; Scharf, M. The Double Cubic Lattice Method: Efficient Approaches to Numerical Integration of Surface Area and Volume and to Dot Surface Contouring of Molecular Assemblies. *Journal of Computational Chemistry* **1995,** *16*, 273-284.

(50) Curley, J. B.; Townsend, T. M.; Bernskoetter, W. H.; Hazari, N.; Mercado, B. Q. Iron, Cobalt, and Nickel Complexes Supported by a Iprpnphp Pincer Ligand. *Organometallics* **2022,** *41*, 301-312.
(51) Groom, C. R.; Bruno, I. J.; Lightfoot, M. P.; Ward, S. C. The Cambridge Structural Database. *Acta Crystallogr B* **2016,** *72*, 171-179.
(52) Duan, C.; Ladera, A. J.; Liu, J. C. L.; Taylor, M. G.; Ariyarathna, I. R.; Kulik, H. J. Exploiting Ligand Additivity for Transferable Machine Learning of Multireference Character across Known Transition Metal Complex Ligands. *Journal of Chemical Theory and Computation* **2022,** *18*, 4836-4845.
(53) Bergstra, J.; Yamins, D.; Cox, D. Making a Science of Model Search: Hyperparameter Optimization in Hundreds of Dimensions for Vision Architectures. *Proceedings of Machine Learning Research* **2013,** *28*, 115-123.
(54) Pedregosa, F.; Varoquaux, G.; Gramfort, A.; Michel, V.; Thirion, B.; Grisel, O.; Blondel, M.; Prettenhofer, P.; Weiss, R.; Dubourg, V. Scikit-Learn: Machine Learning in Python. *Journal of machine learning research* **2011,** *12*, 2825-2830.
(55) Petachem. Http://Www.Petachem.Com/. (Accessed April 17, 2023).
(56) Ufimtsev, I. S.; Martinez, T. J. Quantum Chemistry on Graphical Processing Units. 3. Analytical Energy Gradients, Geometry Optimization, and First Principles Molecular Dynamics. *Journal of Chemical Theory and Computation* **2009,** *5*, 2619-2628.
(57) Lee, C.; Yang, W.; Parr, R. G. Development of the Colle-Salvetti Correlation-Energy Formula into a Functional of the Electron Density. *Physical Review B* **1988,** *37*, 785-789.
(58) Becke, A. D. Density-Functional Thermochemistry. Iii. The Role of Exact Exchange. *Journal of Chemical Physics* **1993,** *98*, 5648-5652.
(59) Stephens, P. J.; Devlin, F. J.; Chabalowski, C. F.; Frisch, M. J. Ab Initio Calculation of Vibrational Absorption and Circular Dichroism Spectra Using Density Functional Force Fields. *The Journal of Physical Chemistry* **1994,** *98*, 11623-11627.
(60) Grimme, S.; Antony, J.; Ehrlich, S.; Krieg, H. A Consistent and Accurate Ab Initio Parametrization of Density Functional Dispersion Correction (Dft-D) for the 94 Elements H-Pu. *The Journal of chemical physics* **2010,** *132*, 154104.
(61) Becke, A. D.; Johnson, E. R. A Density-Functional Model of the Dispersion Interaction. *The Journal of Chemical Physics* **2005,** *123*, 154101.
(62) Johnson, E. R.; Becke, A. D. A Post-Hartree–Fock Model of Intermolecular Interactions. *The Journal of Chemical Physics* **2005,** *123*, 024101.
(63) Johnson, E. R.; Becke, A. D. A Post-Hartree-Fock Model of Intermolecular Interactions: Inclusion of Higher-Order Corrections. *The Journal of Chemical Physics* **2006,** *124*, 174104.
(64) Hay, P. J.; Wadt, W. R. Ab Initio Effective Core Potentials for Molecular Calculations. Potentials for the Transition Metal Atoms Sc to Hg. *The Journal of Chemical Physics* **1985,** *82*, 270-283.
(65) Rappe, A. K.; Casewit, C. J.; Colwell, K. S.; Goddard, W. A., III; Skiff, W. M. Uff, a Full Periodic Table Force Field for Molecular Mechanics and Molecular Dynamics Simulations. *Journal of the American Chemical Society* **1992,** *114*, 10024-10035.
(66) Wang, L.-P.; Song, C. Geometry Optimization Made Simple with Translation and Rotation Coordinates. *The Journal of Chemical Physics* **2016,** *144*, 214108.